3D reconstitution and numerical analysis of superelastic behavior of porous shape memory alloy

Shijie Zhu, Céline Bouby, Abel Cherouat, Tarak Ben Zineb

3D reconstitution and numerical analysis of superelastic behavior of porous shape memory alloy

Shijie Zhu[a], Céline Bouby[b], Abel Cherouat[a], Tarak Ben Zineb[b]

[a] *University of Technology of Troyes, ICD/GAMMA3, F-10010 Troyes, France*
[b] *Université de Lorraine, CNRS, Arts et Métiers ParisTech, LEM3, F-54000 Nancy, France*

Abstract

In this work, a CAD 3D foam structure of Ni-Ti Shape Memory Alloy (SMA) is rebuilt using ellipsoid unit cells in order to study the superelastic behavior of porous SMAs. A taking and placing algorithm based on a uniform and a normal distributions is adopted for the 3D reconstitution process. In the design sample, dimensions, positions and orientations of the ellipsoid unit cells are randomly selected. A SMA constitutive model including phase transformation, martensitic reorientation and twins accommodation is selected to simulate the superelastic behavior of the SMA foam. As an application, the compression of SMA porous sample with random ellipsoid unit cell distribution is simulated by finite element in order to show the efficiency of the proposed methodology to predict its superelastic response and to analyze the porosity effect. The obtained results show that the force-displacement or stress-strain responses of the porous material are highly depend on the foam porosity. The effects of porosity, size, orientation, ratio of long axis and short axis, and distribution of unit cell on the superelastic behavior of SMA porous material are also discussed in both closed cells and open cells cases.

Keywords: Shape Memory Alloy, Foams, 3D reconstitution, Superelasticity

1. Introduction

As a new class of materials, metallic foams have attracted increasing interest in different fields of engineering in the last past decades [1, 2, 3, 4]. These kind

of materials are cellular structures containing solid and gaseous phase, where the cavities occupy a certain percentage of the overall volume. Based on the morphology of their internal cells, the pores can be sealed (closed cell foam) or interconnected (open cell foam). They are particularly versatile because of their interesting mechanical and physical properties: for example, the relatively low density make it possible to obtain a high stiffness/weight ratio, the existence of cavities results in the ability to energy absorption and damping, and also gives them thermal and acoustic insulation properties [1, 2].

As a well-known material for reversible inelastic deformation, Shape Memory Alloys (SMAs) have been paid attention on over last few years [5, 6, 7]. Thanks to the thermoelastic martensitic transformation, SMA materials exhibit two main important properties: superelasticity and shape memory effect. Due to the possibility of these behaviors, it could become interesting if this kind of material can be combined with an attractive structure like porous SMAs. Cellular structures in SMAs are particularly interesting for their potential to provide superelasticity and shape memory effect in a light-weight material. Lot of processes have been investigated to fabricate the SMA foams [8, 9, 10, 11]. Besides, many experiments and characterizations have been done to understand the properties of SMA foams [12, 13, 14]. To complete these experimental data on SMA foams, numerical modeling is needed to predict accurately the properties of this kind of materials. In particular, it might be very useful to study the effective macroscopic behaviors of SMA foams depending on their microstructure. It is obvious that microstructural properties have an influence on macroscopic behaviors, essential for designers, but it is still difficult to derive macroscopic behaviors from microstructure. In this case, computational analyses based on microstructure of porous SMA are undoubtedly necessary.

Some approaches adopted to build the microstructure of porous SMA are based on the assumption of a periodic distribution of pores. Qidwai et al. [15] used the unit cell finite element method (UCFEM) to display periodic distribution of pores in SMA matrix by cutting an in-plane hexagonal arrangement of pores. Sepe et al. [16] have also done some computational micromechanical

analyses of porous SMA to investigate their properties. They used a porous 3D unit cell with transition from spherical to ellipsoidal, then to cylindrical void (at the same time, from closed to open void) and in particular, in terms of the parametric studies, they simplified the model into a 2D one instead. Moreover, Karamooz Ravari et al. [17] used a unit cell model with repetitive pores to simulate the stress-strain response of porous SMA by assuming the porous microstructure as an interpenetration of spheres. However, the assumption of a periodic distribution of pores seems to be far away from the irregularity of real microstructures, which will cause the overestimation of material response. In addition, although the material characteristics can be captured, the approach of Sepe et al. [16] is limited by the fact that only two-dimension model is considered.

In order to create a random model instead of a periodic one, De Giorgi and Qidwai [18] began some researches on mesoscale analysis techniques based on a two-dimensional finite element method, in which pores are allowed to vary in size and shape without limit on maximum pore size. Panico and Brinson [19] used a Representative Volume Element (RVE), by assigning randomly to some elements elastic material properties with negligible stiffness. They also studied another kind of porous SMA in Bewerse et al. [20] with a structured pores obtained starting from scaffold in magnesium. This leads to pores with vertical and horizontal ribbon shape. In addition, Ashrafi et al. [21, 22] and Maîtrejean et al. [23] used a similar RVE approach where the brick element is also randomly picked. These approaches allow to create the irregularity of foam microstructure, however, the irregularity seems not to satisfy the nature smooth and coherent of inner surfaces encountered in the real microstructure.

In this paper, the design of porous structure (open or closed ellipsoid cell), by using a random "taking" and "placing" algorithm and uniform or normal distribution [24], is proposed to build the internal microstructure of porous SMAs. The macroscopic compressive superelastic behavior of NiTi alloy foams is evaluated. In addition of considering an SMA sample with superelastic behavior, the other novelties come from: (i) generating randomly open and closed porous

samples and perform an exhaustive analysis, of the porosity control and optimization (arrangement, size, orientation and volume fraction), (ii) applying the Monte Carlo method in order to predict and optimize the discrete porosity obtained by meshing of the CAD structure, and choosing a normal distribution with a specific limit, (iii) modeling with superelastic thermo-mechanical behavior under loading/unloading for different periodic and random pore distribution considering the effect of their shape, size, and orientation.

For the organization of this paper, section 2 presents the SMA model developed by Duval and Chemisky et al. [25, 26] which is used to predict the thermo-mechanical response of a sample of both closed-cells and open-cells NiTi foams. Section 3.1 shows the procedure of 3D design of foam structure using Monte Carlo and CAD method. In Section 3.2, a numerical simulation of the sample superelastic behavior is presented for a compressive loading-unloading. In Section 4, the effects of porosity, size, orientation, distribution and ratio of long axis and short axis of unit cell on the superelastic behavior of SMA foams are also numerically studied.

2. Constitutive equations of Shape Memory Alloy

In this paper, a constitutive model for SMA including phase transformation, and martensitic reorientation developed by Duval and Chemisky (see [25, 26]) is used to simulate the superelastic behavior of the SMA foam. Thus, two internal variables are defined: the martensite volume fraction f $(0 \leq f \leq 1)$, the mean transformation strain tensor in martensite volume $\overline{\boldsymbol{\varepsilon}}^T$.

The total macroscopic strain tensor can be decomposed as:

$$\boldsymbol{\varepsilon} = \boldsymbol{\varepsilon}^e + \boldsymbol{\varepsilon}^{th} + \boldsymbol{\varepsilon}^T \tag{1}$$

where ($\boldsymbol{\varepsilon}^e$, $\boldsymbol{\varepsilon}^{th}$, $\boldsymbol{\varepsilon}^T$) are respectively the elastic strain, the thermal expansion strain, the inelastic strain due to martensitic transformation.

Further, the equation (1) can be expanded as:

$$\boldsymbol{\varepsilon} = \boldsymbol{S} : \boldsymbol{\sigma} + \boldsymbol{\alpha}(T - T_{ref}) + f\overline{\boldsymbol{\varepsilon}}^T \tag{2}$$

where $\boldsymbol{S}$ is the isotropic fourth order compliance tensor and $\boldsymbol{\sigma}$ is the mean stress tensor, $\boldsymbol{\alpha}$ is the isotropic thermal expansion tensor, T_{ref} is the reference temperature and T is the current temperature.

The derivation of the phenomenological constitutive equations for SMAs begins with the choice of a thermodynamic free energy potential. The Clausius-Duhem inequality can be written in terms of the Gibbs free energy:

$$-\frac{\partial G}{\partial \boldsymbol{\sigma}} : \dot{\boldsymbol{\sigma}} - \frac{\partial G}{\partial T}\dot{T} - \frac{\partial G}{\partial V_k} \cdot \dot{V}_k - \dot{\boldsymbol{\sigma}} : \boldsymbol{\varepsilon} - \vec{q} \cdot \frac{\overrightarrow{gradT}}{T} \geq 0 \tag{3}$$

where V_k are internal variables, $\vec{q}$ is the heat flux vector and the Gibbs free energy potential $G\ (\boldsymbol{\sigma}, T, V_k)$ is defined as follows:

$$\begin{aligned} G =& U^A - TS^A + B(T - T_0)f - \frac{1}{2}\boldsymbol{\sigma} : \boldsymbol{S} : \boldsymbol{\sigma} - \boldsymbol{\sigma} : \boldsymbol{\alpha}(T - T_{ref}) - \boldsymbol{\sigma} : \overline{\boldsymbol{\varepsilon}}^T f \\ &+ \frac{1}{2} f H_\varepsilon \overline{\boldsymbol{\varepsilon}}^T : \overline{\boldsymbol{\varepsilon}}^T + \frac{1}{2} H_f f^2 + C_v \left[(T - T_0) - T \log \frac{T}{T_0} \right] \end{aligned} \tag{4}$$

where $B = -\Delta S = -(S^M - S^A)$, the equilibrium temperature of transformation $T_0 = \frac{\Delta U}{\Delta S} = \frac{U^M - U^A}{S^M - S^A}$ (U^A and U^M are the internal energies of the austenitic and martensitic phases, S^A and S^M are the entropy of the austenitic and martensitic phases), (H_ε and H_f) are constant factors describing interactions between grains and variants, C_v is the heat flux for the RVE.

The force variables linked to internal variables V_k $(f, \overline{\boldsymbol{\varepsilon}}^T)$ are identified as:

- Transformation force linked to f:

$$F_f = -\frac{\partial G}{\partial f} = \boldsymbol{\sigma} : \overline{\boldsymbol{\varepsilon}}^T - B(T - T_0) - \frac{1}{2} H_\varepsilon^T \overline{\boldsymbol{\varepsilon}}^T : \overline{\boldsymbol{\varepsilon}}^T - H_f f \tag{5}$$

- Orientation force linked to $\overline{\boldsymbol{\varepsilon}}^T$:

$$F_{\varepsilon^T} = -\frac{\partial G}{\partial \overline{\boldsymbol{\varepsilon}}^T} = f\boldsymbol{\sigma}^d - f H_\varepsilon^T \overline{\boldsymbol{\varepsilon}}^T \tag{6}$$

Table 1: Summary of the possible cases.

Activated transformation	Activated orientation	Evolution of f and $\overline{\boldsymbol{\varepsilon}}^T$
no	no	$\dot{f} = 0 \quad \dot{\overline{\boldsymbol{\varepsilon}}}^T = 0$
no	yes	$\dot{f} = 0 \quad \dot{\overline{\boldsymbol{\varepsilon}}}^T \neq 0$
yes	yes	$\dot{f} \neq 0 \quad \dot{\overline{\boldsymbol{\varepsilon}}}^T \neq 0$
yes, forward direction	no	$\dot{f} \neq 0 \quad \dot{\overline{\boldsymbol{\varepsilon}}}^T \neq 0$
yes, reverse direction	no	$\dot{f} \neq 0 \quad \dot{\overline{\boldsymbol{\varepsilon}}}^T = 0$

where $\boldsymbol{\sigma}^d$ denotes the deviatoric part of the stress tensor $\boldsymbol{\sigma}$.

The evolution laws of the internal variables can be obtained from the definition of a dissipation potential (see Table. 1):

- For the transformation force:
  - If $|F_f| < F_f^{crit}$ or $|F_f| = F_f^{crit}$ and $|\frac{d|F_f|}{dt}| < 0$, the transformation force is not activated. In this case, the linked variable is constant, therefore $\dot{f} = 0$.
  - If $|F_f| = F_f^{crit}$ and $|\frac{d|F_f|}{dt}| = 0$, the transformation force is activated. In this case, $\dot{f} \neq 0$.

- For the orientation force:
  - If $|F_{\varepsilon^T}| < F_{\varepsilon^T}^{crit}$ or $|F_{\varepsilon^T}| = F_{\varepsilon^T}^{crit}$ and $|\frac{d|F_{\varepsilon^T}|}{dt}| < 0$, there is no orientation. In this case, if the domain does not change, $\dot{\overline{\boldsymbol{\varepsilon}}}^T = 0$. Otherwise, if the domain evolve, $\dot{\overline{\boldsymbol{\varepsilon}}}^T$ evolves to respect the equilibrium.
  - If $|F_{\varepsilon^T}| = F_{\varepsilon^T}^{crit}$ and $|\frac{d|F_{\varepsilon^T}|}{dt}| = 0$, the orientation force is activated. In this case, $\dot{\overline{\boldsymbol{\varepsilon}}}^T \neq 0$.

Table 2 summarizes the constitutive equations which leads to a non linear differential system of first order, solved by the Newton-Raphson scheme as in [27]. The activation of the different specific behaviors of the SMA are detected after an elastic prediction. A corresponding correction is carried out in order to lead to the final behavior.

Table 2: Summary of control equations for the SMA model

Strain mechanisms:

$\boldsymbol{\varepsilon} = \boldsymbol{\varepsilon}^e + \boldsymbol{\varepsilon}^{th} + \boldsymbol{\varepsilon}^T$

Thermodynamical potential:

$G = U^A - TS^A + B(T - T_0)f - \frac{1}{2}\boldsymbol{\sigma} : \boldsymbol{S} : \boldsymbol{\sigma} - \boldsymbol{\sigma} : \boldsymbol{\alpha}(T - T_{ref}) - \boldsymbol{\sigma} : \overline{\boldsymbol{\varepsilon}}^T f + \frac{1}{2} f H_\varepsilon \overline{\boldsymbol{\varepsilon}}^T : \overline{\boldsymbol{\varepsilon}}^T$

$+ \frac{1}{2} H_f f^2 + C_v \left[(T - T_0) - T \log \frac{T}{T_0} \right]$

Clausius-Duhem inequality:

$-\frac{\partial G}{\partial \boldsymbol{\sigma}} : \dot{\boldsymbol{\sigma}} - \frac{\partial G}{\partial T}\dot{T} - \frac{\partial G}{\partial V_k} \cdot \dot{V}_k - \dot{\boldsymbol{\sigma}} : \boldsymbol{\varepsilon} - \vec{q} \cdot \frac{\overrightarrow{gradT}}{T} \geq 0$

Thermo-elastic balance conditions:

$\boldsymbol{S} : \boldsymbol{\sigma} + \boldsymbol{\alpha}(T - T_{ref}) + f\overline{\boldsymbol{\varepsilon}}^T - \boldsymbol{\varepsilon} = 0$

$S^A - fB + \boldsymbol{\sigma} : \boldsymbol{\alpha} - C_v \left(\log \frac{T}{T_0} \right) = 0$

Thermodynamics forces:

$F_f = -\frac{\partial G}{\partial f} = \boldsymbol{\sigma} : \overline{\boldsymbol{\varepsilon}}^T - B(T - T_0) - \frac{1}{2} H_\varepsilon^T \overline{\boldsymbol{\varepsilon}}^T : \overline{\boldsymbol{\varepsilon}}^T - H_f f$

$F_{\varepsilon^T} = -\frac{\partial G}{\partial \overline{\boldsymbol{\varepsilon}}^T} = f\boldsymbol{\sigma}^d - f H_\varepsilon^T \overline{\boldsymbol{\varepsilon}}^T$

Criterion functions:

$|F_f| \leq F_f^{yield}$

$|F_{\varepsilon^T}| \leq f F_{\varepsilon^T}^{yield}$

It is worth mentioning that the SMA model has been implemented in ABAQUS via user's material UMAT, which allows us to carry out the simulations by FE on the sample.

3. Numerical analysis of shape memory NiTi foams

In this section, an iterative 3D reconstitution of foam structure using CAD method is detailed, which will be used for numerical analysis of superelastic behavior of porous SMA sample under compression load.

3.1. 3D reconstitution of foam structure

The sample contains a series of ellipsoids with random variable ranges: dimension, position and orientation. Each ellipsoid is located randomly. In order to not repeat again the existing position, a specific checking method of intersection is developed. Two conditions should be taken into consideration: firstly, the ellipsoid to be checked must be intersected with at least one of the existing valid ellipsoids; secondly, the intersecting part of the two ellipsoids should not occupy a large part of the existing valid ellipsoids because of the foam structure authenticity. The real porosity was estimated by the analysis of digital images of flat sections of a given microstructure. By the fact, pores dimensions and distribution in the flat section is assumed to be close to the real tridimensional one for a random pore distributions and sizes. Based on the obtained random sizes and distribution of pores, the realistic microstructure statistical distribution is performed.

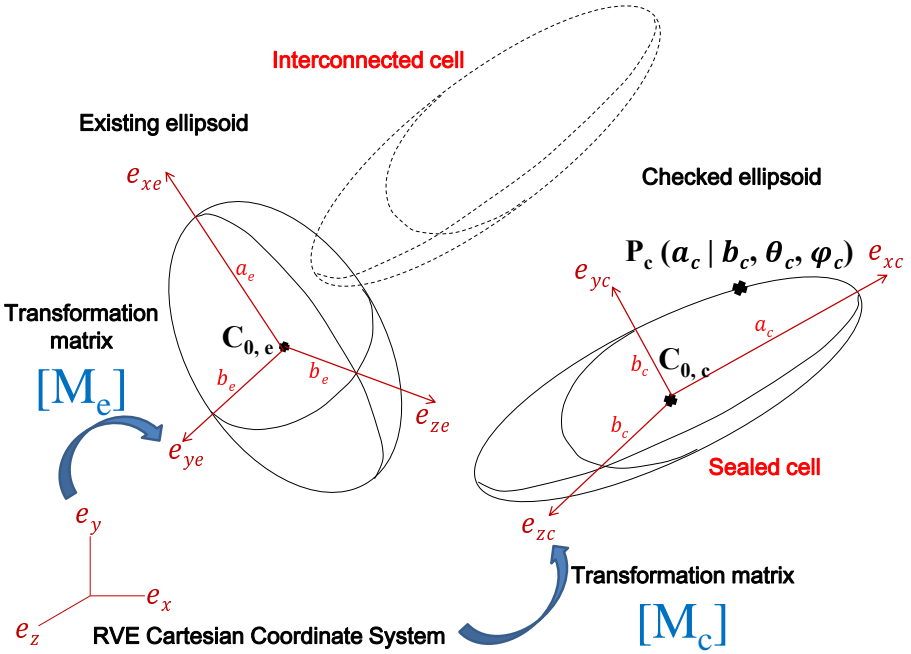

Figure 1: The ellipsoids with geometrical parameters.

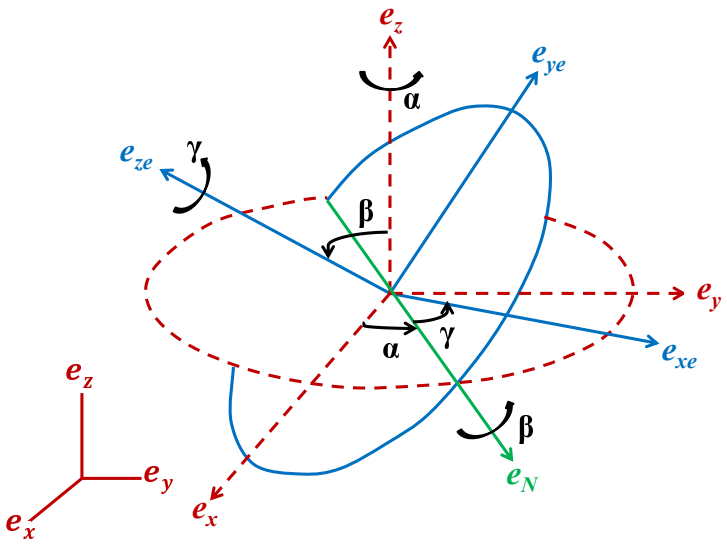

Figure 2: Orientation angles of the ellipsoids.

In order to build porous structure with random cell morphology, an ellipsoid shape where two of the three axes are the same is used to define the foam pore using the following parameters (see Fig. 1):

Position: C_0 (x_0, y_0, z_0) are the coordinates of the ellipsoid center;

Dimension: (a, b) are the lengths of the semi-major and the semi-minor axis;

Orientation: (α, β, γ) are the orientation angles of the ellipsoid (Euler angles) (see Fig. 2).

The flowchart of the geometric modeling of foams with random distributions of ellipsoidal cells using MATLAB and Abaqus/CAE is shown on Fig. 3. The basic steps of the taking and placing algorithm are described thereafter.

Step 1 **Definition of porous sample ellipsoid characteristics**

To obtain a foam structure, we define a series of ellipsoids with random variable ranges: dimension, position and orientation.

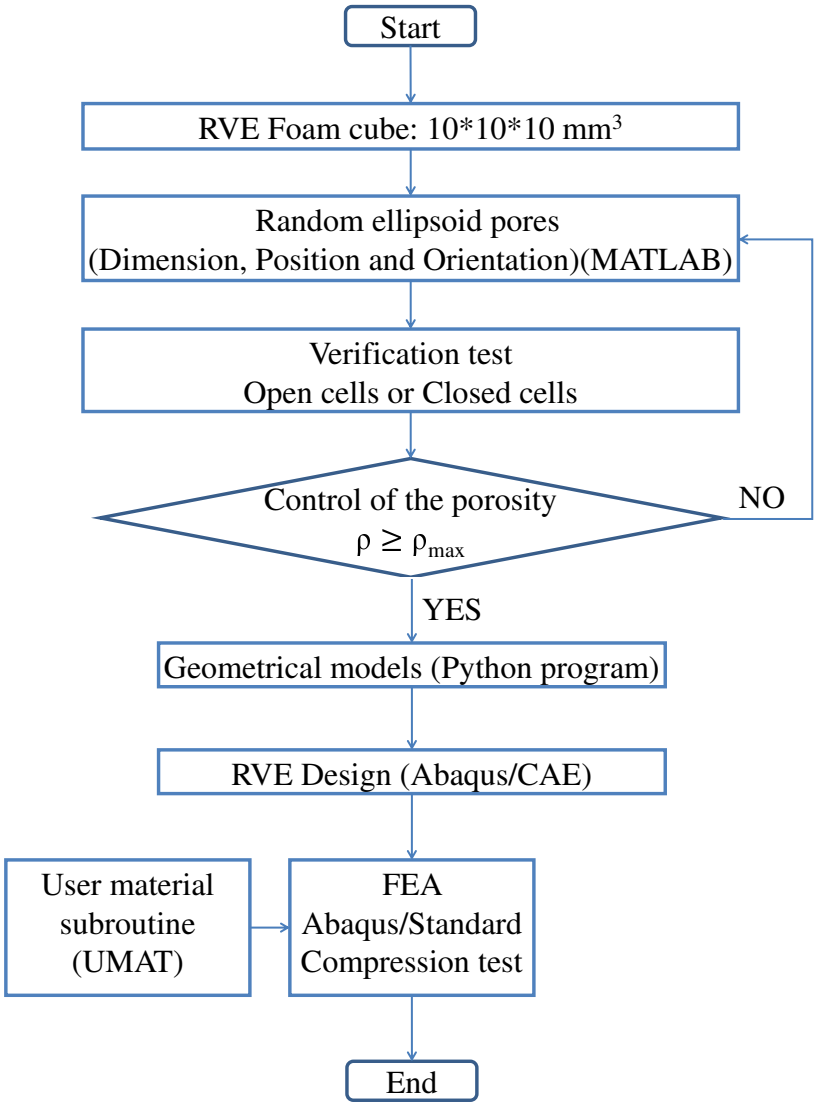

Figure 3: Flowchart of foam modeling with random distributions of ellipsoid pores.

The sample chosen is a cube of dimension $10 \times 10 \times 10\ mm^3$. Therefore, the coordinates of the ellipsoid center C_0 can be fixed from 0 to 10 mm

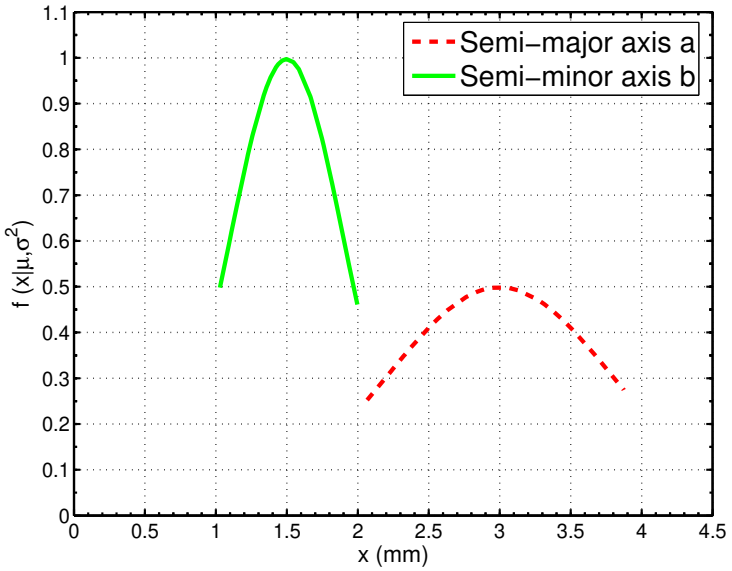

Figure 4: Normal distribution for a specific limit for a and b.

by a uniform distribution.

A normal distribution with a specific limit is chosen for $(a,\ b)$. Thus, we can define a's normal distribution $a \sim N(3, 0.8^2)$, and a's range $a \in (2, 4)$; b's normal distribution $b \sim N(1.5, 0.4^2)$, and b's range $b \in (1, 2)$ (see Fig. 4). In the figure, $f(x \mid \mu, \sigma^2)$ is the probability density of the normal distribution, which shows the probability of the appearance for the corresponding values of a and b. Within the probability density, μ is the mean of the distribution, σ^2 is the variance.

Finally, orientation angles α and γ are range in $[-\pi, \pi]$, and β is range in $[0, \pi]$.

Step 2 **Verification test** (open cells or closed cells)

During the process of generating foam structure, first, an ellipsoid unit cell is set up in the sample cube, and then the next introduced ellipsoids are examined whether they meet the conditions to form open cells or closed cells. Therefore, there are always two kinds of unit cell: the existing valid

ellipsoids and the ellipsoid to be checked.

In this part, only open cells are considered because closed cells can be considered as a special case of open cells. To this end, a method of intersection checking is developed. Two conditions should be taken into consideration: firstly, the ellipsoid to be checked must be intersected with at least one of the existing valid ellipsoids; secondly, the intersecting part of the two ellipsoids should not occupy a large part of the existing valid ellipsoid because of the foam structure authenticity. On the basis of these two conditions, the points on the surface of the ellipsoid to be checked are used to verify whether and how much the ellipsoid to be checked intersects with the existing valid ellipsoid. The coordinates of each point P, using spherical coordinate system of the ellipsoid to be checked (e_{xc}, e_{yc} and e_{zc}), are defined as (see Fig. 1):

$$\begin{cases} x_c = a_c \cos\theta_c \\ y_c = b_c \sin\theta_c \cos\varphi_c \\ z_c = b_c \sin\theta_c \sin\varphi_c \end{cases} \tag{7}$$

where θ_c is the polar angle and φ_c the azimuth angle, (a_c, b_c) are positive real numbers.

Considering that the ellipsoid to be checked and the existing valid ellipsoid have different coordinate systems, based on their standard ellipsoid equations, the coordinate transformation related to the orientation angles of the ellipsoid (α, β, γ) is definitely needed. The transformation matrix is defined from the coordinate system of the sample cube (e_x, e_y and e_z) to that of the ellipsoid to be checked (e_{xc}, e_{yc} and e_{zc}) as $[M_c]$, and that from the sample cube (e_x, e_y and e_z) to the existing valid ellipsoid (e_{xe}, e_{ye} and e_{ze}) as $[M_e]$ (see Fig. 1 and Fig. 2). It should be noticed that the matrices $[M_c]$ and $[M_e]$ can be derived from the definition of the ellipsoid as the orientation angles (Euler angles) are well known for every ellipsoid. The relation between the transformation matrix $[M_c]$ or $[M_e]$

and the orientation angles (α, β, γ) are:

$$[M_c] \; or \; [M_e] = \begin{bmatrix} M_{11} & M_{12} & M_{13} \\ M_{21} & M_{22} & M_{23} \\ M_{31} & M_{32} & M_{33} \end{bmatrix}$$

$$\begin{cases} M_{11} = \cos\alpha\cos\gamma - \sin\alpha\cos\beta\sin\gamma \\ M_{12} = \cos\alpha\sin\gamma - \sin\alpha\cos\beta\cos\gamma \\ M_{13} = \sin\alpha\sin\beta \\ M_{21} = -\sin\alpha\cos\gamma - \cos\alpha\cos\beta\sin\gamma \\ M_{22} = -\sin\alpha\sin\gamma + \cos\alpha\cos\beta\cos\gamma \\ M_{23} = \cos\alpha\sin\beta \\ M_{31} = \sin\beta\sin\gamma \\ M_{32} = -\sin\beta\cos\gamma \\ M_{33} = \cos\beta \end{cases} \tag{8}$$

Therefore, the coordinates of the ellipsoid to be checked after transformation are:

$$\begin{bmatrix} x_e \\ y_e \\ z_e \end{bmatrix} = [M_e]^{-1} \left[[M_c] \begin{bmatrix} x_c \\ y_c \\ z_c \end{bmatrix} + \begin{bmatrix} x_{0,c} - x_{0,e} \\ y_{0,c} - y_{0,e} \\ z_{0,c} - z_{0,e} \end{bmatrix} \right] \tag{9}$$

where $C_{0,c}$ ($x_{0,c}$, $y_{0,c}$, $z_{0,c}$) and $C_{0,e}$ ($x_{0,e}$, $y_{0,e}$, $z_{0,e}$) are respectively the coordinates of the ellipsoid centers in the sample coordinate system (see Fig. 1).

The verification is done using the equation:

$$\xi = \frac{x_e^2}{a_e^2} + \frac{y_e^2}{b_e^2} + \frac{z_e^2}{b_e^2} \tag{10}$$

If $\xi < 1$, the point P on the surface of the ellipsoid to be checked is inside the existing valid ellipsoid. By setting the range $-\frac{\pi}{2} < \theta < \frac{\pi}{2}$,

$-\pi \leq \varphi < \pi$, and the spacing as $\frac{2\pi}{64}$, 1984 points to be tested are created for one ellipsoid to be checked. Here, only 200 points are considered as the upper limit for the intersecting of the ellipsoid to be checked and the existing valid ellipsoid. This is a compromise between computational time of porous foam reconstruction and validation of intersection of the ellipsoid to be checked.

Step 3 **Control of the porosity**

It is difficult to calculate exactly the porosity of open cells foam even if all the parameters of the ellipsoid unit cells are known. It is due to the complexity of the intersections between two ellipsoids.

To solve this problem, a statistical method is used to approximate the porosity. First, a point P_p (x_p, y_p, z_p) is generated randomly inside the sample cube by a uniform distribution. Then using the coordinate transformation, the coordinates of P_p in the coordinate system of the existing valid ellipsoid (e_{xe}, e_{ye} and e_{ze}) is:

$$\begin{bmatrix} x_{pe} \\ y_{pe} \\ z_{pe} \end{bmatrix} = [M_e]^{-1} \begin{bmatrix} x_p - x_{0,e} \\ y_p - y_{0,e} \\ z_p - z_{0,e} \end{bmatrix} \tag{11}$$

and the equation for verification is:

$$\xi_p = \frac{x_{pe}^2}{a_e^2} + \frac{y_{pe}^2}{b_e^2} + \frac{z_{pe}^2}{b_e^2} \tag{12}$$

If $\xi_p < 1$, then the point P_p is inside of the existing valid ellipsoid. In this way, we note the successful index S as 1, otherwise we note S as 0.

Furthermore, the Monte Carlo method is applied to predict the porosity [28]. Precisely, a large number of the times to generate P_p is executed, here we define it as 10000. By calculating how many times T in the situation where S equals 1, and by calculating $\frac{T}{10000}$, the porosity of foam structure could be well approximated.

Step 4 **Numerical models**

On the basis of the secondary development of Abaqus language script Python, by repeating the process of generating ellipsoid pores, the foam structure is built on the following steps:

For the detailed steps:

Iteration 1 A cube of sample is built (see Fig. 3).

Iteration 2 Three points inside the cube are chosen randomly to constitute a plane of sketch. The coordinates of these points are used to calculate the orientation angles (α, β, γ) in order to satisfy the conditions discussed above.

Iteration 3 An approximate semi ellipse is drawn in the plane of sketch by using (a, b). By executing revolved cut in the cube, an ellipsoid pore can be generated.

By repeating the iterations 2 and 3 for every existing valid ellipsoid unit cell, the whole foam structure CAD is finally constructed.

Fig. 5 reports the level steps of a foam CAD reconstitution with 30 pores and the tetrahedral finite element mesh of porous sample using Optiform software [29, 30, 31, 32] .

3.2. FEM model and boundary conditions

Numerical simulation of super-elastic porous sample response under a compression loading-unloading and a constant temperature involves the use of the finite element analysis. It allows to compute, for each applied external load increment, the successive new body configurations verifying the equilibrium equations as well as the constitutive equations accounting for the above discussed coupled mechanical phenomena. For SMAs it consider phase transformation, martensitic reorientation. A contact with friction is considered between each rigid plane and one of the both horizontal sample edges (see Fig. 6). One of the rigid planes is fixed where the second is moved with control of the vertical

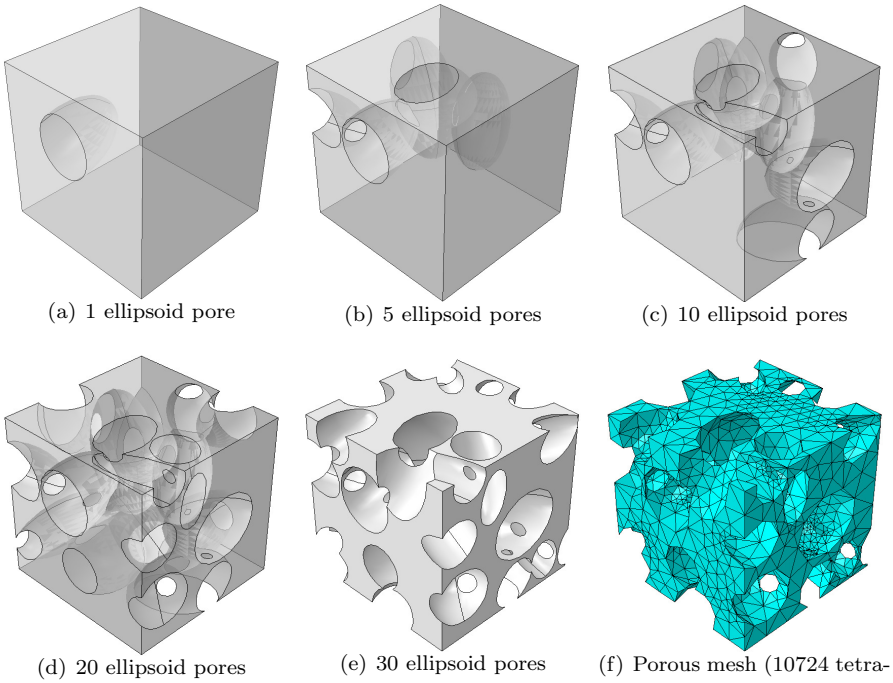

(a) 1 ellipsoid pore (b) 5 ellipsoid pores (c) 10 ellipsoid pores

(d) 20 ellipsoid pores (e) 30 ellipsoid pores (f) Porous mesh (10724 tetrahedral elements)

Figure 5: Evolution of the sample morphology in function of the number of pores (a) to (e) and adapted porous structure mesh (f).

displacement. It consists to incrementally apply a displacement u=1.5mm during loading and unloading. Its horizontal displacement is assumed to be equal to zero. This defines a non-linear Initial and Boundary Value Problem based on the Updated Lagrangian description, which needs to be incrementally linearized in order to find the roots using an iterative implicit scheme. All the examples presented herein have been obtained with Abaqus/Implicit thanks to the use of the developed UMAT user subroutine describing the SMA thermos-mechanical behavior. Our main goal is to illustrate the capability of the proposed methodology to predict the superelastic response of a porous SMA structure (effective stiffness, volume fraction of martensite evolution, forces in both loading and unloading and the dissipated energy) during isothermal and quasi-static compression. The two rigid planes was modeled by two discrete rigid surfaces using

4-node rigid shell elements (R3D4). A surface-to-surface contact with friction ($\mu = 0.1$) was introduced to model the interaction between the platen and the specimen. The porous NiTi SMA structure with different porosities has a dimension of 10mm×10mm×10mm and is discretized by deformable continuum linear tetrahedral finite elements (C3D4). The thermomechanical material parameters, detailed in [26], are adopted to study the superelasticity of the porous SMA at the austenitic initial state. Therefore, the mechanical loading/unloading under a constant temperature of $T = 30°C$ is simulated by Abaqus Implicit.

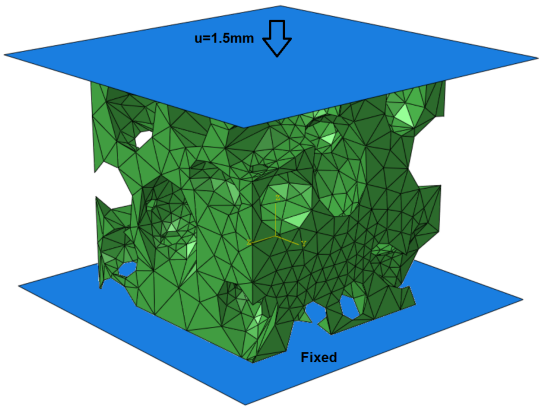

Figure 6: FEM model and boundary conditions

3.3. Numerical analysis of superelastic behavior

The predicted compression loading and unloading force versus displacement results obtained by the proposed methodology are presented in Fig. 7. We can notice that a typical form of the superelastic behavior response of a porous SMA is observed. Several key points, including the effective stiffness k_{slope} (the slope of the line), some important forces in both loading and unloading procedure (the points A, B, C and D) and the dissipated energy (the area of the curve), are chosen here to reveal the superelastic behavior of porous SMA, which will be studied in the following sections. Fig. 8 presents the volume fraction of martensite for different tool displacements. It can be seen that at the largest compression level displacement, almost all of the sample are transformed.

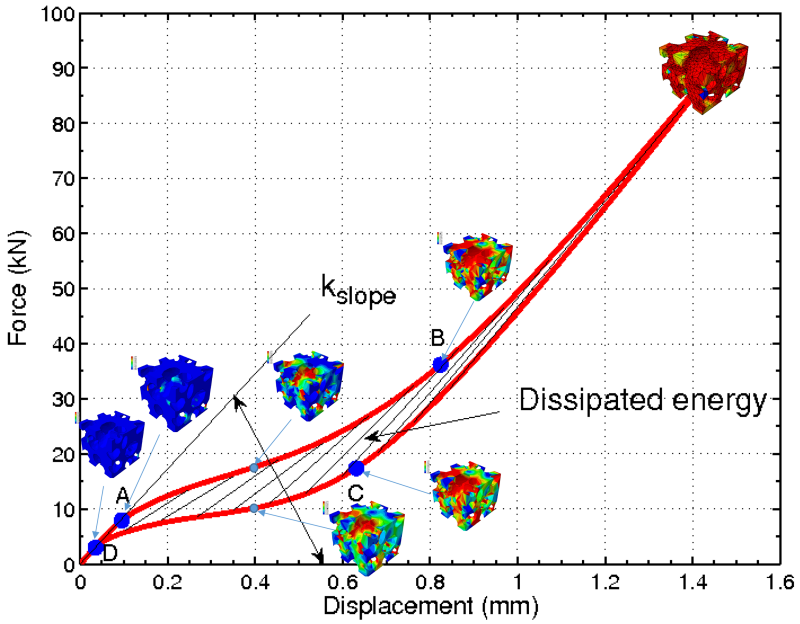

Figure 7: Force-displacement response.

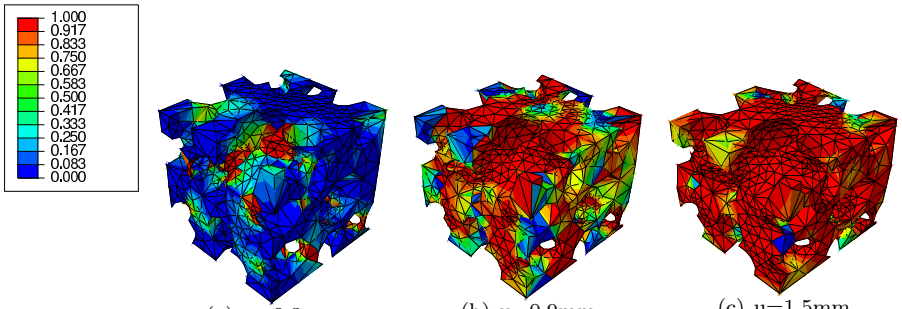

(a) u=0.3mm (b) u=0.9mm (c) u=1.5mm

Figure 8: Volume fraction of martensite for different compression displacements.

4. SMA foam parameters study

Considering the fact that the performance of porous materials can be affected by the pore shape, size, distribution and orientation, different simulations are carried out to study these effects on the overall response of the sample. Here,

the studies on both open cells and closed cells (see Fig. 9) are investigated and compared with other results published in [16], [17] and [34].

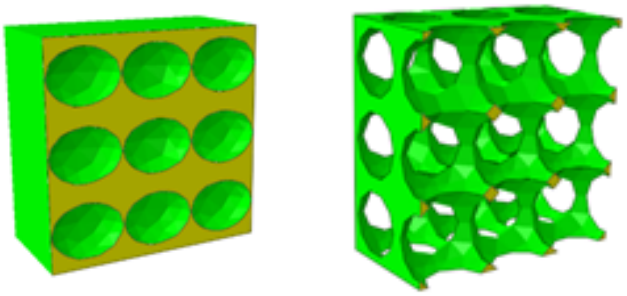

(a) Closed cell (b) Open cell

Figure 9: Studied pores morphology

As the porosity volume fraction depends on the mesh of foam CAD, the mesh is controlled here according to the quality of the elements, the geometric curvatures of the surfaces of the pores and the gradation of the mesh inside the domain. The real porosity of the discrete CAD of the cell foam depends on the mesh size. If the mesh is fine then the porosity changes very little but the calculation time is very important. We adopt the meshes according to the desired porosity, the quality of the elements and the computation times. The table 3 shows the error between the real porosity and the discrete porosity for open and closed foams. We can note that for the proposed mesh in this paper, the average error is of the order of 7% for open cells and 11% for closed cells. The samples are meshed by home developed tool and is applied to each sample with a given volume fraction porosity leading to specific mesh for each sample.

4.1. Porosity effect of random foams

4.1.1. Open cell foam

In this section, the predicted compression loading and unloading force for different porosity values, $\rho = 0$ (bulk), 40, 60, 70 and 80% respectively, is presented. In Fig. 10, some typical points named A, B, C and D are chosen

Table 3: Summary of the possible cases.

CAD Porosity	Discrete porosity Open cell foam	Discrete porosity Closed cell foam
20%	18.23% Error: 8.8%	17.68% Error: 11.61 %
30%	27.08% Error: 9.72%	26.59% Error: 11.37%

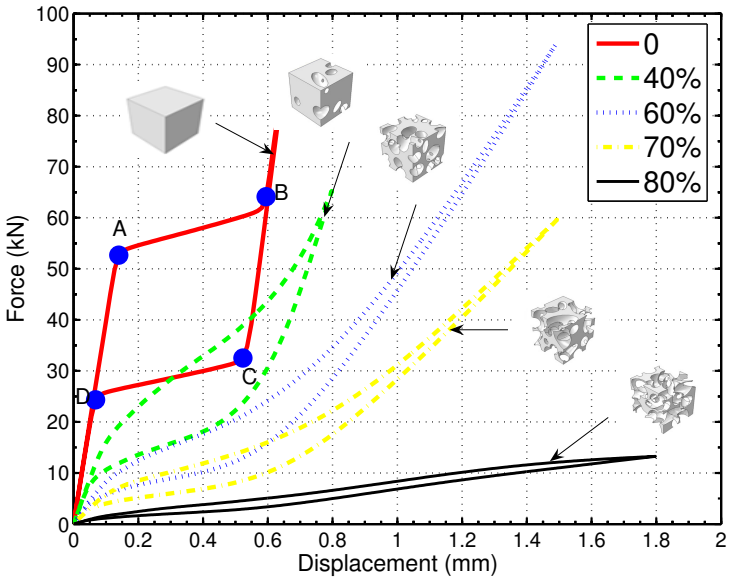

Figure 10: Compressive force vs displacement for different porosities of open cells.

during the loading and unloading procedure. In this figure, the points A and B show respectively the start and the finish of forward transformation from Austenite to Martensite during loading, while the points C and D show the start and the finish of reverse transformation from Martensite to Austenite during unloading. The Table. 4 shows the important parameters for different porosities for open cells. Also, it is observed that for porous SMA structure, the transition from elastic to phase transformation behavior is smoother than that of bulk one. This phenomenon is due to the inhomogeneity of stress distribution

Table 4: Important parameters for different porosities for open cells.

Porosity	0	40%	60%	70%	80%
Maximum displacement (mm)	0.65	0.8	1.5	1.5	1.8
Effective stiffness k_{slope} (kN/mm)	395.5	175.5	88.5	61.3	18.2
Dissipated energy (N×m)	13.1	7.7	5.6	4.9	2.2
Force in Point A (kN)	52.7	15.1	8.0	5.7	1.4
Force in Point B (kN)	64.1	46.6	36.2	25.9	12.1
Force in Point C (kN)	34.8	27.0	17.4	12.5	3.7
Force in Point D (kN)	24.6	6.9	3.0	2.6	0.6

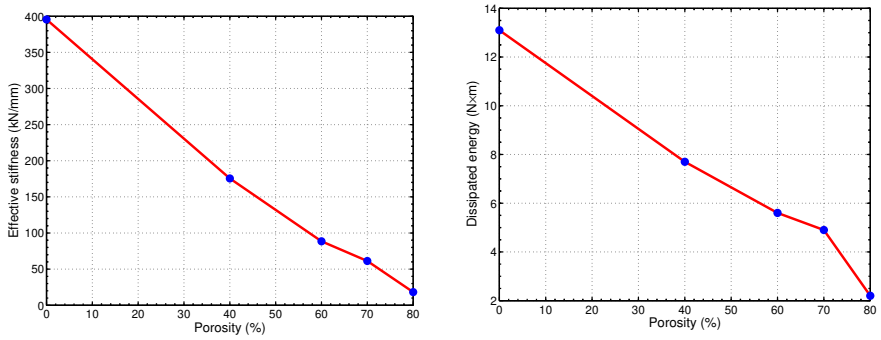

(a) Effective stiffness

(b) Dissipated energy

Figure 11: The effect of porosity on the SMA open cell foam on (a) effective stiffness and (b) dissipated energy.

in porous SMAs. The Fig. 11 shows that with the increasing of porosity, the effective stiffness k_{slope} and the dissipated energy decrease. This is easy to understand because less material in total leads to less macroscopic stress. In addition, it can be seen that the hardening rate in phase transformation region increases with the increase of porosity. This is due to the reduction of the ratio of stresses for the beginning and the end of martensitic transformation as well as the elastic modulus. According to [17], the increase of the porosity also leads to the increase of the stress concentration around the pores, which results in strain localization. Consequently, in order to obtain a specific strain value, smaller

macroscopic stress for larger porosity is required, which demonstrates a smaller hardening rate. Another reason is that the increase of the porosity causes the reduction of martensite and austenite elastic modulus, resulting in the decrease of the total stiffness of the material. All the obtained results show the same tendency as those of the references [16] and [17].

4.1.2. Closed cell foam

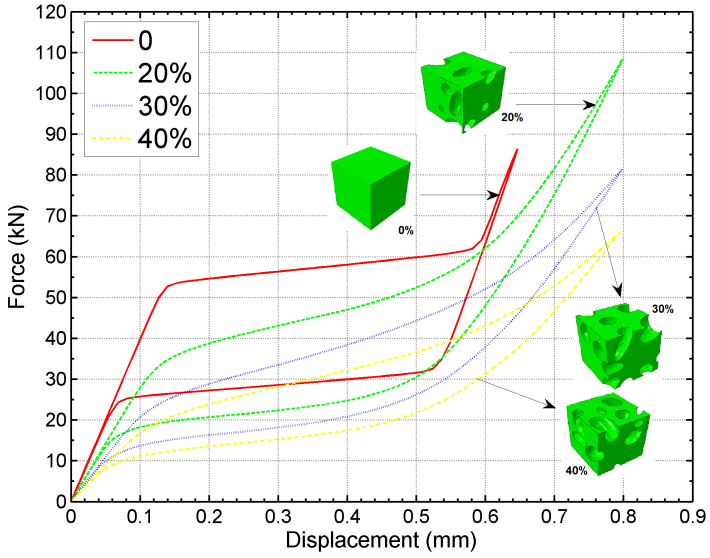

Figure 12: Compressive force vs displacement for different porosities of closed cells.

Fig. 12 shows the predicted loading and unloading compression force-displacement curves for different random porosity values of closed cells, $\rho = 0$ (bulk), 20, 30, 40% respectively. It should be noticed that, according to the distribution theory, the maximum porosity of the random closed cell model is about 50% [35]. The obtained results imply that the porosity of the porous material affects the mechanical properties of foam structure in term of stiffness, flexibility and damping (see Table. 5). It shows the similar tendencies observed with the open cells, which are: the decreasing of the effective stiffness, the forces in typical points (A, B, C and D) and the dissipated energy with the increasing of porosity.

Table 5: Important parameters for different porosities for closed cells.

Porosity	0%	20%	30%	40%
Maximum displacement (mm)	0.65	0.8	0.8	0.8
Effective stiffness k_{slope} (kN/mm)	395.5	280.0	213.3	175.0
Dissipated energy (N×m)	13.1	11.2	9.1	7.6
Force in Point A (kN)	52.7	30.7	19.3	15.1
Force in Point B (kN)	64.1	60.3	56.2	42.3
Force in Point C (kN)	34.8	32.1	29.6	22.7
Force in Point D (kN)	24.6	12.5	8.2	7.1

These first results concern the open or closed cell sample foams in which the size, orientation, distribution, and ratio of long axis and short axis are random. It should be noticed that for the effects of these parameters, a periodic structure is more appropriate to exploit the results. Accordingly, the unit cell will be arranged periodically in the whole sample for every foam structure in the following to investigate the superelastic behavior.

4.2. Pore size effect of periodic foam

4.2.1. Open cell foam

For a periodic structure porous SMA with constant porosity $\rho = 80\%$, three unit cell sizes (a = 7.51, 3.76 and 2.50 mm) of the long axis (see Fig. 13) are studied numerically. Fig. 14 shows the predicted compression force-displacement curves. The results during both loading and unloading, show that when the long axis a decreases (which corresponds to a reduction of the size of unit cell), the effective stiffness and the forces in typical points (A, B, C and D) both increase. This could be explained by a decrease of the unit cell size leading to an increase of the stress localization around the pores of high porosity of foam (80%). In fact, our conclusion shows a greatly difference with that in [17] in which the foam porosity is very small (13%).

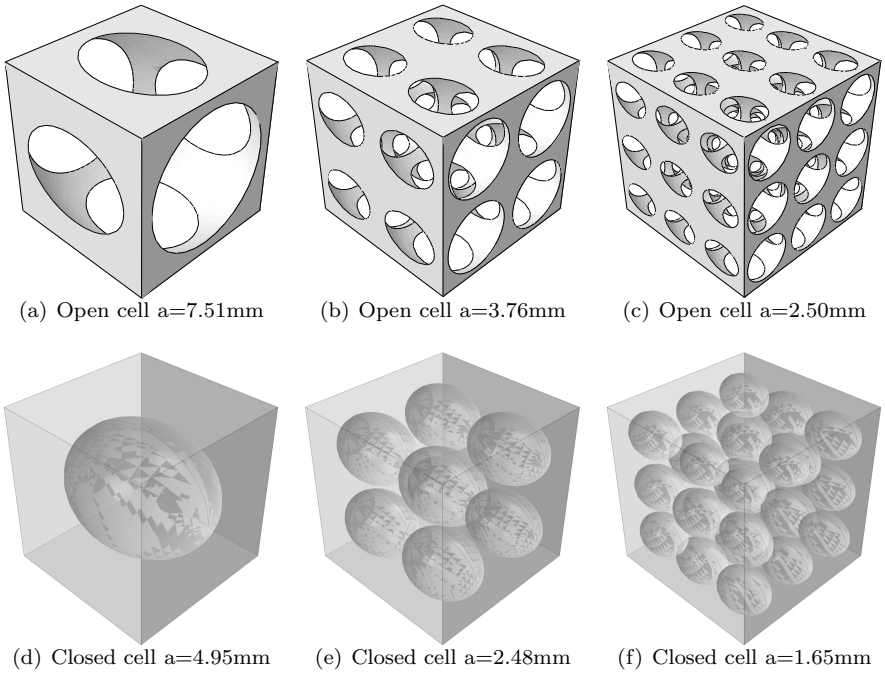

(a) Open cell a=7.51mm (b) Open cell a=3.76mm (c) Open cell a=2.50mm

(d) Closed cell a=4.95mm (e) Closed cell a=2.48mm (f) Closed cell a=1.65mm

Figure 13: CAD structure of open (a) to (c) and closed (d) to (f) foams for three unit cell sizes of the long axis.

4.2.2. Closed cell foam

In this section, the sample porosity is $\rho = 30\%$ and three unit cell sizes of the long axis (a = 4.95, 2.48 and 1.65 mm) of porous SMA (see Fig. 13) are investigated numerically. The obtained results of the predicted compression loading and unloading force-displacement allow to infer that in the closed cells, the long axis size of the periodic unit cell has no significant effect on the effective stiffness, the forces in typical points and the dissipated energy (see Fig. 15).

4.3. Pore axial ratio effect of periodic foam

4.3.1. Open cell foam

The effect of the ratio of long axis and short axis of periodic foam ($r = a/b$) is also studied for open cells ($\rho = 80\%$). Fig. 17 shows that the obtained predicted force-displacement curves for different ratio values, r = 1 (sphere), r

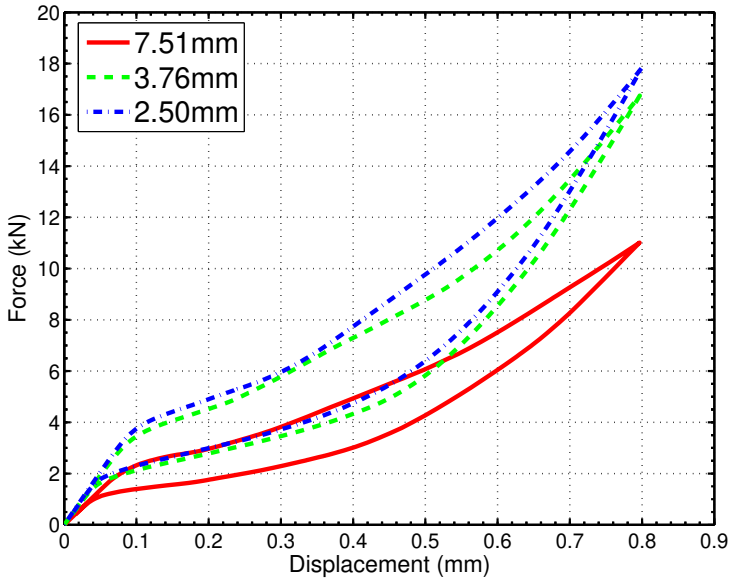

Figure 14: Compressive force vs displacement for different size values of open cells.

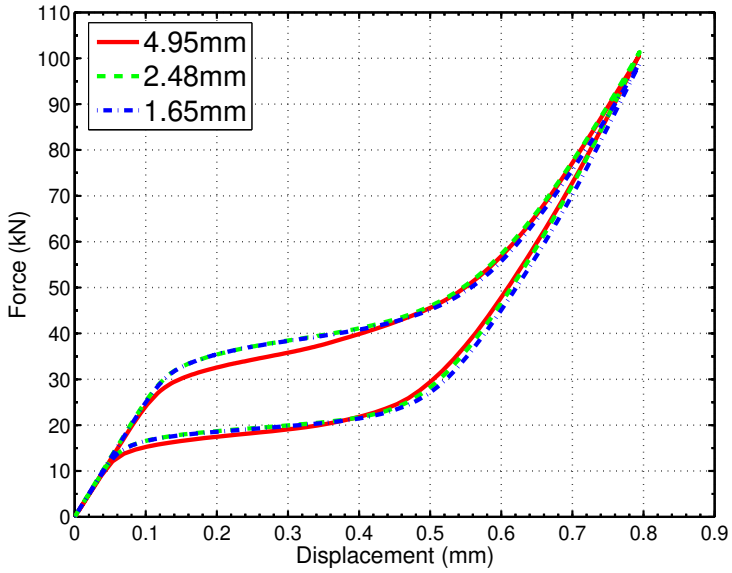

Figure 15: Compressive force vs displacement for different size values of closed cells.

= 1.15 and r = 1.3 (ellipse) respectively (see Fig. 16). According to the results, the ratio r affects the effective stiffness and the forces in typical points. The

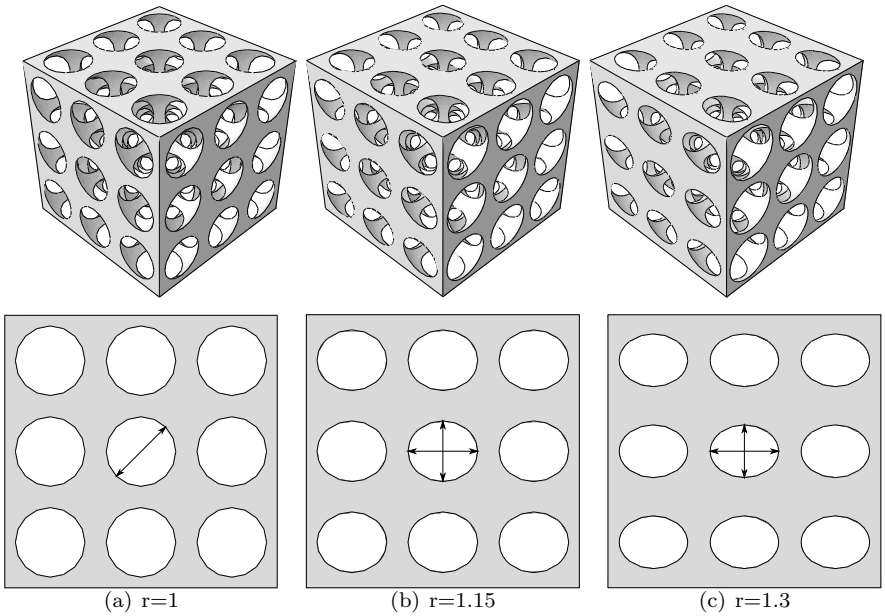

(a) r=1 (b) r=1.15 (c) r=1.3

Figure 16: The whole structure and the main view (in the X-Y plan) of three ratios of unit cell.

results can be compared with those in [16] and [34] even though they use only one unit cell resulting in the SMA foam with low porosity. Indeed, our results show the same trend as those of the references [16] and [34]. This could be explained by the increase of the ratio of long axis and short axis which leads to the increase of the stress concentration (estimated at about 5000 MPa, see Fig. 18). The difference should come from the fact that the direction of long axis of elliptical pores is orthogonal to that of the imposed displacement. Therefore, for the foam with higher ratio, the forward/reverse transformation occurs for a lower stress, resulting in a lower stress in the start and the finish of the forward/reverse transformation (points A, B, C and D). It is worth mentioning that this explanation is supported by the reference [34], where the distributions of the martensitic volume fraction show that the sample, with a higher ratio, presents the earliest starting martensitic transformation.

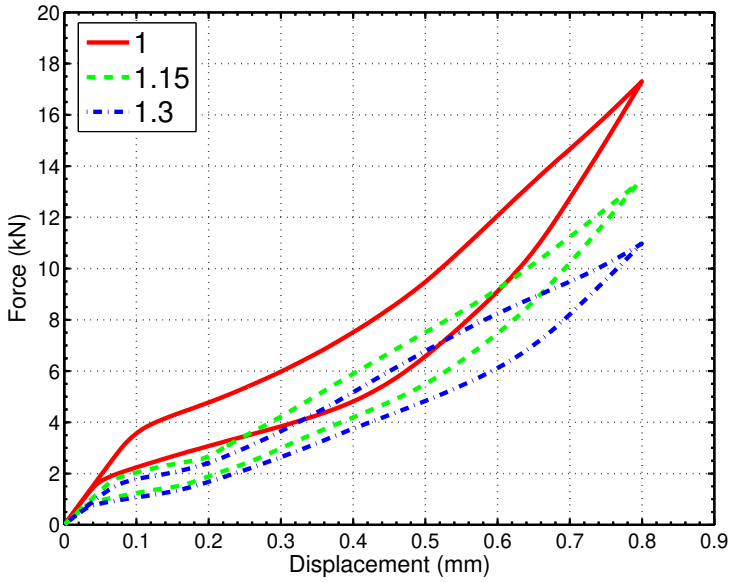

Figure 17: Compressive force-displacement responses for different ratio of long and short axis of open cells.

4.3.2. Closed cell foam

In this section, the effect of the ratio is investigated for closed periodic cell foam. Fig. 19 displays the obtained predicted force-displacement curves for different ratio values, r = 1 (sphere), r = 1.15 and r = 1.3 (ellipse) respectively. The results reflect that the ratio of long axis and short axis does not have an apparent effect on the overall performance of SMA foams in the case of closed cells. In order to better investigate the effect on the internal structure, the distributions of the martensite volume fraction at the end of loading (0.8 mm) for the three ratios are shown in Fig. 20. It can be seen that for the three samples with different ratios, most parts of them have completed the martensite transformation, while for some areas between the pores in the horizontal direction and the areas in the bottom, the martensite transformation just starts. If we consider the distribution of the martensite volume fraction in the main view (in the X-Y plan) for the three samples, it can be observed that there is not a big difference among them, which might proves that, the effect of the ratio is not

apparent for closed cells.

4.4. Pore orientation effect of periodic foam

4.4.1. Open cell foam

In order to study the effect of the orientation of unit cell pore, the angle between the directions of long axis and the horizontal directions is defined by an angle θ. The periodic model with the same porosity (ρ = 80%), same size (a = 2.50 mm) and same ratio (r = 1.3) is used (see Fig. 21). Fig. 22 displays the numerical compressive force-displacement curves for different orientations $\theta = 0^o$, 45^o and 90^o respectively. Based on these results, one can note that, the increase of the orientation leads to an increase of the effective stiffness and the forces in typical points. It can be observed that, with the increase of the orientation, the length of pores in the longitudinal direction (here defined as a') decreases, while that in the transverse direction (here defined as b') increases (see Fig. 21). From this point of view, the study of the orientation effect can be regarded as that of the effect of long axis' and short axis' varieties. Thus, our results can be compared with those in [16] and [34], which provide the cases $a' > b'$ and $a' < b'$ corresponding to the orientations 0^o and 90^o. The result presented in the references [16] and [34] show the similar tendencies.

4.4.2. Closed cell foam

In this section, the porosity of the periodic model is set at ρ =30%. The results of the numerical compressive response (see Fig. 23) indicate that, in the case of closed cells, the effective stiffness and the forces in typical points are slightly affected by the orientation of unit cell pores. The distributions of the martensite volume fraction at the end of loading for the three orientations are also investigated and shown in Fig. 24. It can be observed from the figure that the regions of completed martensite transformation grow slightly with the increase of the orientation. The regions of uncompleted martensite transformation occur at the bottom of the samples and in the vicinity of the pores with the arrangement in the transverse direction. The sample with more completed

martensite transformation regions shows higher stiffness, which can well explain that the curve associated to the orientation of 90^o is slightly above that of 45^o, and that of the orientation of 45^o is slightly above that of 0^o. In fact, this phenomenon can be also found in open periodic foams. The difference between the open cells and the closed cells is the obvious effect of the orientation on the open cells, while on the closed cells it is slight.

4.5. Pore distribution of periodic foam

In this section, three cases of pore distributions of open unit cell are considered (see Fig. 25):

- Evenly distribution (case (a));
- Unevenly distribution in transverse direction (case (b));
- Unevenly distribution in longitudinal direction (case (c)).

Fig. 26 shows the obtained predicted force-displacement curves for the three different types of distribution, from case 1 to case 3. According to the results, in both loading and unloading steps, the effective stiffness and the forces in typical points in case 1 are higher than those in cases 2 and 3. The reason could be that the inhomogeneity of pore distribution in cases 2 and 3 causes an increasing of the stress concentration, which makes their effective stiffness and forces lower than those of homogeneous pore distribution case 1. Here, it can be said that case 3 (bigger pore size in the longitudinal direction) is less influenced by the transverse loading direction than case 2 (bigger pore size in the transverse direction).

Table 6: Comparison of the effects for both open and closed cells.

Parameter effects	Porosity	Size	Orientation	Ratio	Distribution
Open cells	Obvious	Obvious	Obvious	Obvious	Obvious
Closed cells	Obvious	Slight	Slight	Slight	Slight

Table. 6 summarizes all the observations on the effects of size, orientation, distribution, and ratio of long axis and short axis of unit cell into consideration for both closed cells and open cells. From the Table. 6, it can be inferred clearly that the parametric effect of foam with open cells is significant, whereas with closed cells is less. This statement is of great interest because it clearly shows that the superelastic behavior of porous SMA also depends on whether the unit cells intersect with each other or not. It exhibits that the connectivity of unit cell in the foam structure is also an important parameter for the performance of this kind of material, which in addition provides the idea for foam structure design.

5. Conclusion

A study of 3D foam microstructure reconstitution and behavior has been carried out. The open or closed foam structure, its porosity (which can be controlled), is well built on the basis of the ellipsoid unit cell pores with random dimension, position and orientation. Constitutive equations of superelastic behavior are used to simulate the compression of porous shape memory alloys.

The obtained results indicate that the porosity is a crucial parameter to characterize SMA foams for both closed and open cells. When the foam porosity increases, the effective stiffness, the forces in the start and the finish of forward and reverse transformation (between Austenite and Martensite) and the dissipation energy decrease.

The effects of size, ratio of long axis and short axis, orientation and distribution of unit cell pores on the response of loading and unloading compression are studied numerically for open and closed foams. For open cells particularly, the effective stiffness, the forward and reverse transformation forces and the dissipated energy increase with the decrease of size, the increase of orientation and the decrease of ratio of long axis and short axis of ellipsoid pores. For the distributions, the situation shows different results. This might be due to the effects of 'the transverse direction' and 'the longitudinal direction'. However,

for closed cells, the effects of pore geometry, dimension and distribution are not significant on foam mechanical responses.

The mechanical analysis from the microstructure of porous SMA material provide us a better understanding of this kind of structure, which is used for the design of some specified devices demanding the advantage of porous SMA. Precisely, this article could provide good ideas for the designer in terms of porosity, size, orientation, shape and distribution for SMA open cell foams.

Concerning our future work, the effect of interaction between unit cells for porous SMA will be investigated in order to explain the difference of the size, orientation, distribution and ratio effects between open and closed cells. In addition, since the parameter effect study considered in this article focuses mainly on the periodic model, it could be an interesting topic to understand how the parameter effects act on the random porous SMA model, which will be also a part of our future work.

Acknowledgements

This work is supported by the China Scholarship Council (CSC).

References

References

[1] L. J. Gibson, M. F. Ashby, Cellular solids: structure and properties, Cambridge University Press, 1999 (1999).

[2] M. F. Ashby, T. Evans, N. A. Fleck, J. Hutchinson, H. Wadley, L. Gibson, Metal foams: a design guide, Elsevier, 2000 (2000).

[3] V. Deshpande, N. Fleck, Isotropic constitutive models for metallic foams, Journal of the Mechanics and Physics of Solids 48 (6) (2000) 1253–1283 (2000).

[4] S. Forest, J.-S. Blazy, Y. Chastel, F. Moussy, Continuum modeling of strain localization phenomena in metallic foams, Journal of Materials Science 40 (22) (2005) 5903–5910 (2005).

[5] K. Otsuka, C. M. Wayman, Shape memory materials, Cambridge University Press, 1999 (1999).

[6] D. C. Lagoudas, Shape memory alloys: modeling and engineering applications, Springer Science & Business Media, 2008 (2008).

[7] C. Lexcellent, Shape-memory alloys handbook, John Wiley & Sons, 2013 (2013).

[8] A. Bansiddhi, D. C. Dunand, Shape-memory NiTi foams produced by solid-state replication with NaF, Intermetallics 15 (12) (2007) 1612–1622 (2007).

[9] A. Bansiddhi, D. Dunand, Shape-memory NiTi foams produced by replication of NaCl space-holders, Acta Biomaterialia 4 (6) (2008) 1996–2007 (2008).

[10] E. Castrodeza, C. Mapelli, M. Vedani, S. Arnaboldi, P. Bassani, A. Tuissi, Processing of shape memory CuZnAl open-cell foam by molten metal infiltration, Journal of Materials Engineering and Performance 18 (5-6) (2009) 484–489 (2009).

[11] A. Bansiddhi, D. C. Dunand, Processing of NiTi foams by transient liquid phase sintering, Journal of Materials Engineering and Performance 20 (4-5) (2011) 511–516 (2011).

[12] S. Nemat-Nasser, Y. Su, W.-G. Guo, J. Isaacs, Experimental characterization and micromechanical modeling of superelastic response of a porous NiTi shape-memory alloy, Journal of the Mechanics and Physics of Solids 53 (10) (2005) 2320–2346 (2005).

[13] S. Wu, C. Y. Chung, X. Liu, P. K. Chu, J. Ho, C. Chu, Y. Chan, K. Yeung, W. Lu, K. Cheung, et al., Pore formation mechanism and characterization

of porous NiTi shape memory alloys synthesized by capsule-free hot isostatic pressing, Acta Materialia 55 (10) (2007) 3437–3451 (2007).

[14] O. Scalzo, S. Turenne, M. Gauthier, V. Brailovski, Mechanical and microstructural characterization of porous NiTi shape memory alloys, Metallurgical and Materials Transactions A 40 (9) (2009) 2061–2070 (2009).

[15] M. A. Qidwai, P. B. Entchev, D. C. Lagoudas, V. G. De Giorgi, Modeling of the thermomechanical behavior of porous shape memory alloys, International Journal of Solids and Structures 38 (48) (2001) 8653–8671 (2001).

[16] V. Sepe, F. Auricchio, S. Marfia, E. Sacco, Micromechanical analysis of porous SMA, Smart Materials and Structures 24 (8) (2015) 085035 (2015).

[17] M. K. Ravari, M. Kadkhodaei, A. Ghaei, A unit cell model for simulating the stress-strain response of porous shape memory alloys, Journal of Materials Engineering and Performance 24 (10) (2015) 4096–4105 (2015).

[18] V. G. De Giorgi, M. A. Qidwai, A computational mesoscale evaluation of material characteristics of porous shape memory alloys, Smart Materials and Structures 11 (3) (2002) 435 (2002).

[19] M. Panico, L. Brinson, Computational modeling of porous shape memory alloys, International Journal of Solids and Structures 45 (21) (2008) 5613–5626 (2008).

[20] C. Bewerse, L. C. Brinson, D. C. Dunand, Porous shape-memory niti-nb with microchannel arrays, Acta Materialia 115 (2016) 83–93 (2016).

[21] M. Ashrafi, J. Arghavani, R. Naghdabadi, S. Sohrabpour, A 3-D constitutive model for pressure-dependent phase transformation of porous shape memory alloys, Journal of the Mechanical Behavior of Biomedical Materials 42 (2015) 292–310 (2015).

[22] M. Ashrafi, J. Arghavani, R. Naghdabadi, S. Sohrabpour, F. Auricchio, Theoretical and numerical modeling of dense and porous shape memory

alloys accounting for coupling effects of plasticity and transformation, International Journal of Solids and Structures 88 (2016) 248–262 (2016).

[23] G. Maîtrejean, P. Terriault, V. Brailovski, Density dependence of the superelastic behavior of porous shape memory alloys: representative volume element and scaling relation approaches, Computational Materials Science 77 (2013) 93–101 (2013).

[24] M. De Giorgi, A. Carofalo, V. Dattoma, R. Nobile, F. Palano, Aluminium foams structural modelling, Computers & Structures 88 (1) (2010) 25–35 (2010).

[25] A. Duval, M. Haboussi, T. Ben Zineb, Modelling of localization and propagation of phase transformation in superelastic SMA by a gradient nonlocal approach, International Journal of Solids and Structures 48 (13) (2011) 1879–1893 (2011).

[26] Y. Chemisky, A. Duval, E. Patoor, T. Ben Zineb, Constitutive model for shape memory alloys including phase transformation, martensitic reorientation and twins accommodation, Mechanics of Materials 43 (7) (2011) 361–376 (2011).

[27] Y. Chemisky, A. Duval, B. Piotrowski, T. Ben Zineb, V. Tahiri, E. Patoor, Numerical tool for SMA material simulation: application to composite structure design, Smart Materials and Structures 18 (10) (2009) 104012 (2009).

[28] M. A. Reichenberger, R. G. Fronk, J. K. Shultis, J. A. Roberts, N. S. Edwards, S. R. Stevenson, C. N. Tiner, D. S. McGregor, Monte Carlo simulation of random, porous (foam) structures for neutron detection, Radiation Physics and Chemistry 130 (2017) 186–195 (2017).

[29] H. Borouchaki, T. Grosges, D. Barchiesi, Enhancement of the accuracy of numerical eld computation using an adaptive three-dimensional remeshing scheme, C.R. Mec. (2010).

[30] H. Borouchaki, T. Grosges, D. Barchiesi, Improved 3d adaptive remeshing scheme applied in high electromagnetic field gradient computation, Finite Elem. Anal. Des. 46 (2010) 8495 (2010).

[31] J. Zhang, A. Cherouat, H. Borouchaki, 3d thermo-mechanical simulation coupled with adaptive remeshing for metal milling, Adv. Mater. Res. 698 (2013) 1120 (2013).

[32] A. Cherouat, H. Borouchaki, Z. J., Simulation of sheet metal forming processes using a fully rheological-damage constitutive model coupling and a specific 3d remeshing method, Metals 8 (12) (2018) 991 (2018).

[33] P. Sittner, L. Heller, J. Pilch, P. Sedlak, M. Frost, Y. Chemisky, A. Duval, B. Piotrowski, T. Ben Zineb, E. Patoor, et al., Roundrobin SMA modeling (2009) 08001 (2009).

[34] P. F. Dehaghani, S. H. Ardakani, H. Bayesteh, S. Mohammadi, 3D hierarchical multiscale analysis of heterogeneous SMA based materials, International Journal of Solids and Structures 118 (2017) 24–40 (2017).

[35] R. D. Kamien, A. J. Liu, Why is random close packing reproducible?, Physical Review Letters 99 (15) (2007) 155501 (2007).

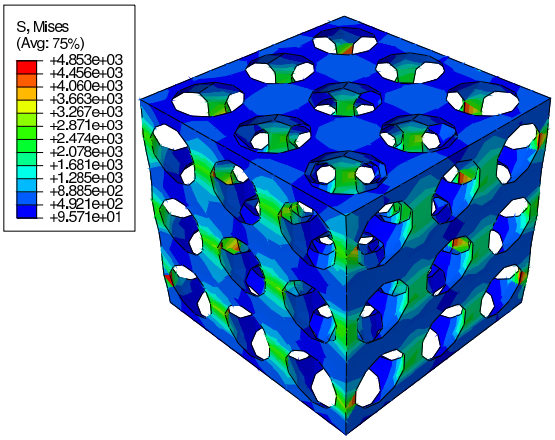

(a) r=1

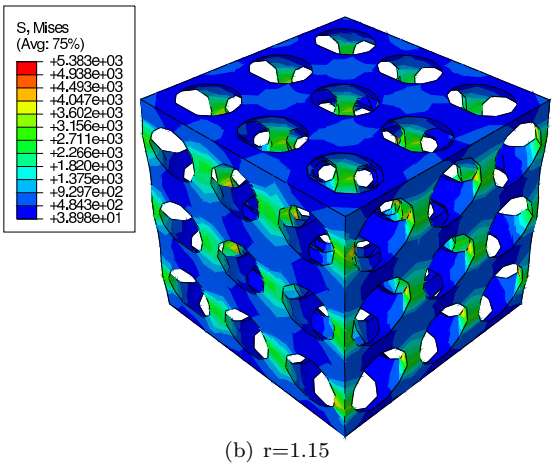

(b) r=1.15

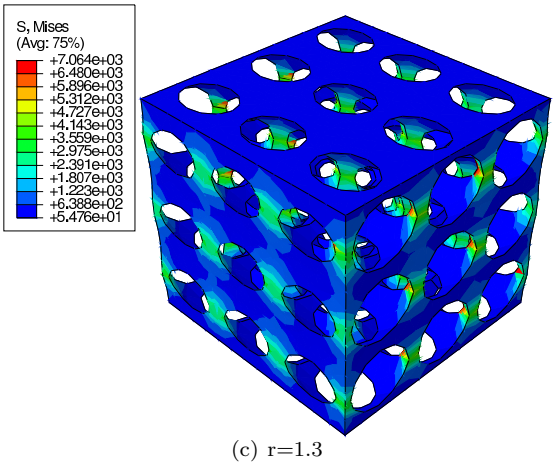

(c) r=1.3

Figure 18: Distribution of the stress at the end of loading for three ratios of unit cell.

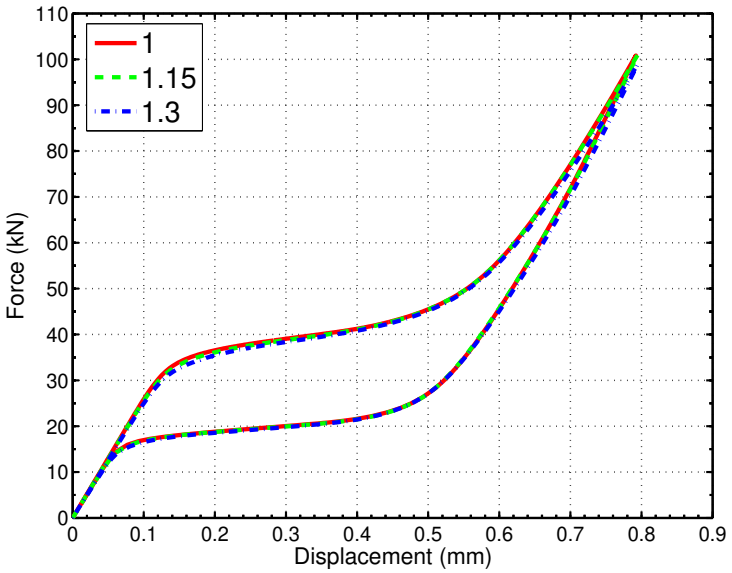

Figure 19: Compressive force-displacement responses for different ratio of long and short axis of closed cells.

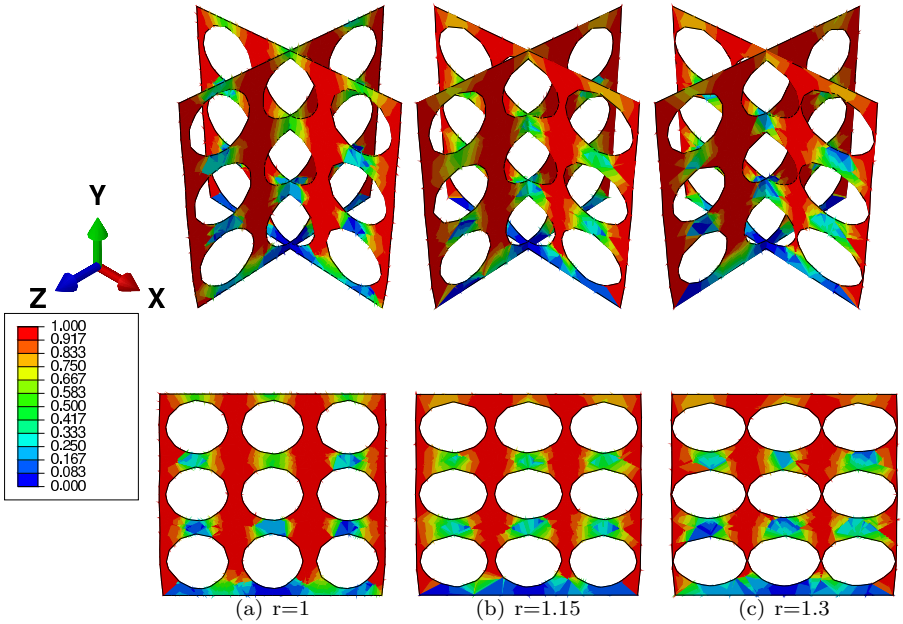

(a) r=1 (b) r=1.15 (c) r=1.3

Figure 20: Distribution of the martensite volume fraction at the end of loading for three ratios of unit cell.

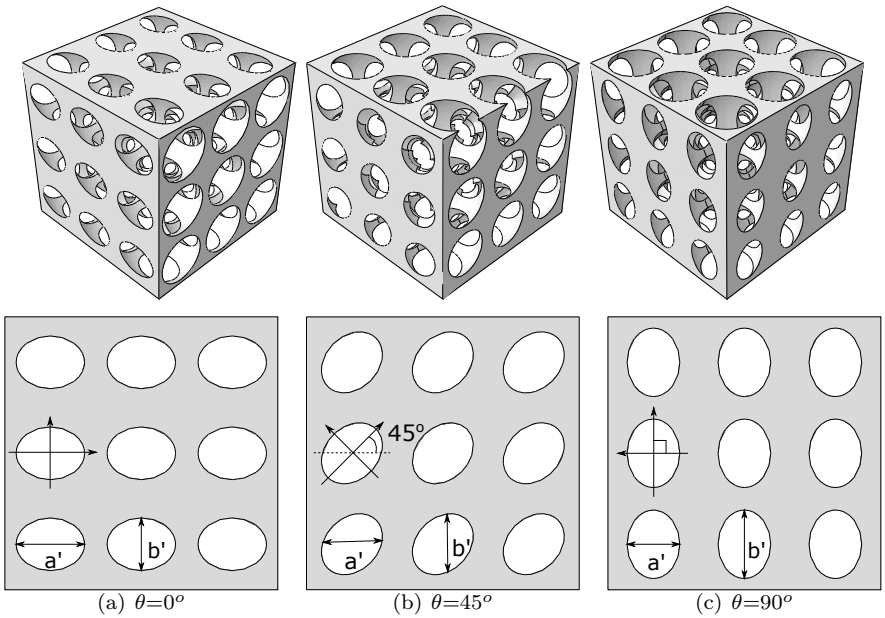

(a) θ=0^o (b) θ=45^o (c) θ=90^o

Figure 21: The whole structure and the main view (in the X-Y plan) of three orientations of unit cell.

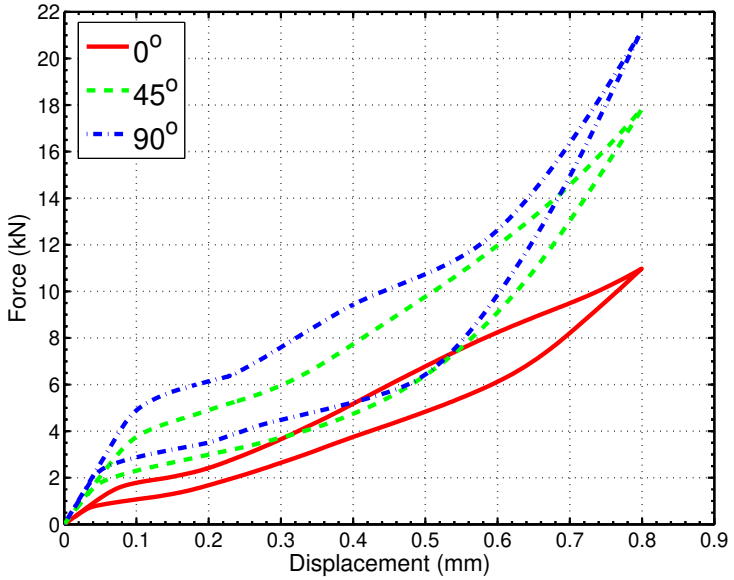

Figure 22: Compressive force-displacement responses for different orientation values of open cells.

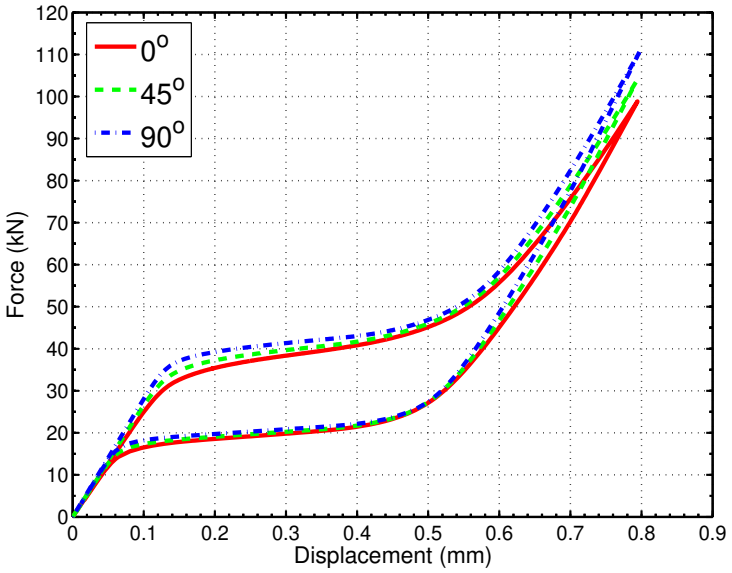

Figure 23: Compressive force-displacement responses for different orientation values of closed cells.

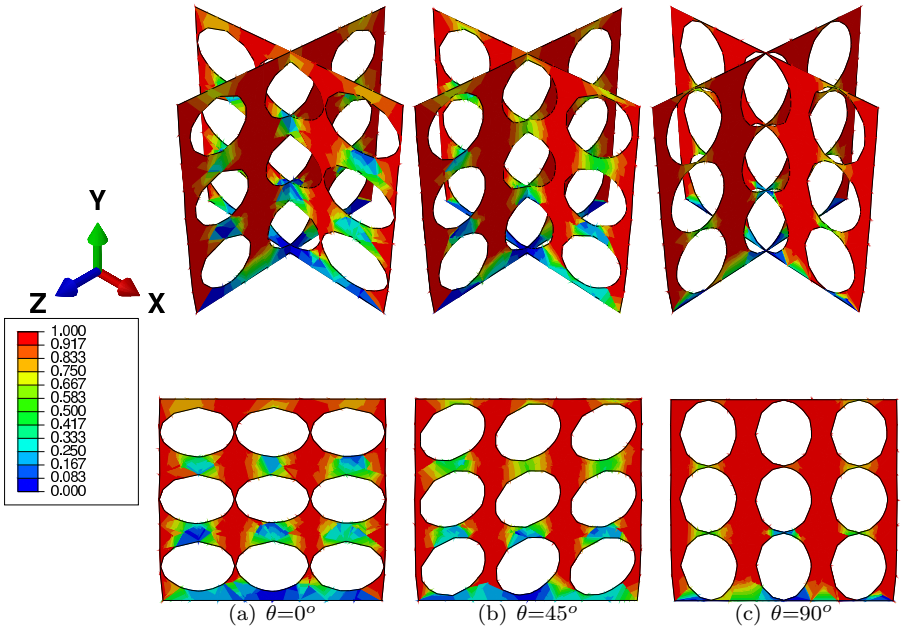

(a) θ=0^o (b) θ=45^o (c) θ=90^o

Figure 24: Distribution of the martensite volume fraction at the end of loading for three orientations of unit cell.

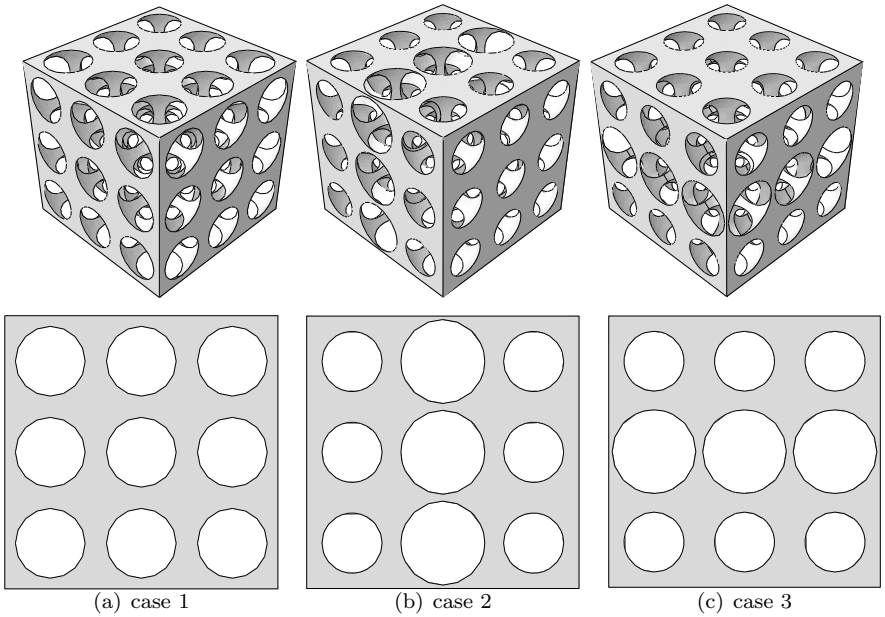

(a) case 1 (b) case 2 (c) case 3

Figure 25: The whole structure of three types of distribution of unit cell.

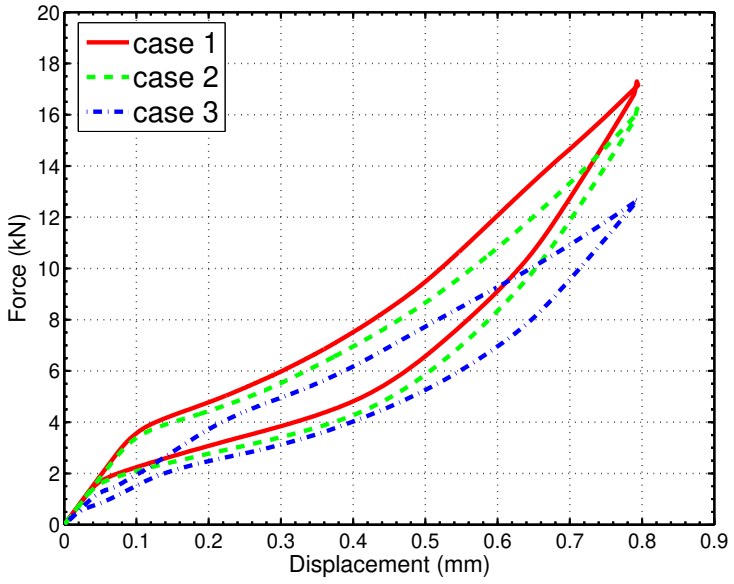

Figure 26: Compressive force-displacement responses for different types of distribution of open cells.